

# A diamond nanophotonic interface with an optically accessible deterministic electronuclear spin register

Received: 10 May 2023

Accepted: 13 October 2023

Published online: 13 November 2023

 Check for updates

Ryan A. Parker<sup>1,3</sup>, Jesús Arjona Martínez<sup>1,3</sup>, Kevin C. Chen<sup>2</sup>, Alexander M. Stramma<sup>1</sup>, Isaac B. Harris<sup>2</sup>, Cathryn P. Michaels<sup>1</sup>, Matthew E. Trusheim<sup>2</sup>, Martin Hayhurst Appel<sup>1</sup>, Carola M. Purser<sup>1</sup>, William G. Roth<sup>1</sup>, Dirk Englund<sup>2</sup>✉ & Mete Atatüre<sup>1</sup>✉

A contemporary challenge for the scalability of quantum networks is developing quantum nodes with simultaneous high photonic efficiency and long-lived qubits. Here we present a fibre-packaged nanophotonic diamond waveguide hosting a tin-vacancy centre with a spin-1/2 <sup>117</sup>Sn nucleus. The interaction between the electronic and nuclear spins results in a signature 452(7) MHz hyperfine splitting. This exceeds the natural optical linewidth by a factor of 16, enabling direct optical nuclear spin initialization with 98.6(3)% fidelity and single-shot readout with 80.0(1)% fidelity. The waveguide-to-fibre extraction efficiency of our device of 57(6)% enables the practical detection of five-photon events. Combining the photonic performance with the optically initialized nuclear spin, we demonstrate a spin-gated single-photon nonlinearity with 11(1)% contrast in the absence of an external magnetic field. These capabilities position our nanophotonic interface as a versatile quantum node in the pursuit of scalable quantum networks.

Scalable quantum networking motivates the search for a platform with simultaneous access to a high-quality high-efficiency optical interface and to long-lived memory qubits<sup>1</sup>. Commonly, the choice of the material platform presents a trade-off between these independent requirements. Self-assembled quantum dots stand out for their photonic quality and integration maturity<sup>2,3</sup>, which has enabled the demonstrations of near-deterministic spin-photon interactions<sup>4</sup>, remote entanglement<sup>5</sup> and cluster-state generation<sup>6</sup>. The intrinsically limited spin coherence<sup>7</sup> and the lack of an easily accessible long-lived register<sup>8</sup> have hindered their potential for long-distance quantum networking. This is in stark contrast to the nitrogen-vacancy centre in a diamond, which sustains an impressive degree of spin coherence<sup>9</sup> and provides access to long-lived nuclear memories<sup>10</sup>. However, spectral instability and low-rate

coherent-photon emission<sup>11</sup> remains an obstacle for scaling up quantum networks<sup>12</sup>.

The negatively charged group-IV colour centres in a diamond (silicon vacancy (SiV), germanium vacancy (GeV) and tin vacancy (SnV)) span this gap, as they possess both high-quality optical properties<sup>13–15</sup> and long spin-coherence times<sup>16,17</sup>. Long-lived nuclear memories can be realized through hyperfine coupling to stochastically present <sup>13</sup>C (ref. 18). Alternatively, the nuclear host spin may be employed, as demonstrated for SiV (ref. 19), and has the advantage of a stronger and deterministic coupling.

The recent success of group-IV colour centres lies in their ease of integration into photonic waveguides<sup>14,15,20</sup> and nanocavities<sup>18,20–22</sup>. This is attributed to their centro-symmetry, and therefore, they are insensitive to surface electrical noise. Building on the pioneering role

<sup>1</sup>Cavendish Laboratory, University of Cambridge, Cambridge, UK. <sup>2</sup>Department of Electrical Engineering and Computer Science, Massachusetts Institute of Technology, Cambridge, MA, USA. <sup>3</sup>These authors contributed equally: Ryan A. Parker, Jesús Arjona Martínez. ✉e-mail: [englund@mit.edu](mailto:englund@mit.edu); [ma424@cam.ac.uk](mailto:ma424@cam.ac.uk)

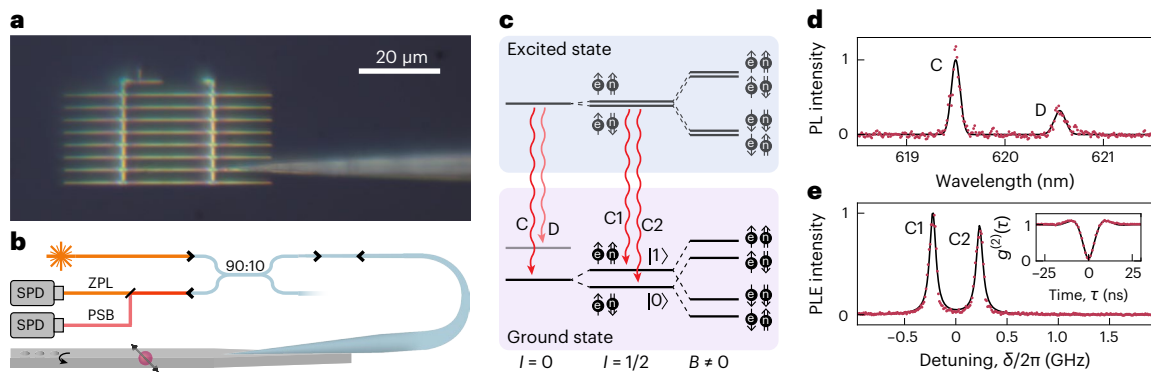


**Fig. 1 | A nanophotonic quantum device hosting an electronuclear spin register.** **a**, Microscopy photograph of the packaged device. An ultraviolet-cured optical adhesive permanently fixes the tapered fibre after it is contacted onto a diamond microchiplet. **b**, Experimental setup. We excite the emitter near resonance and collect both PSB fluorescence and resonant reflection (ZPL) light into the single-photon detectors (SPDs). **c**, Electronic structure of the SnV centre. The hyperfine coupling between the electron (e) and  $^{117}\text{Sn}$  nucleus (n) results in a splitting of the optical transition at zero magnetic field. A non-zero magnetic

field further splits the two electronic states. **d**, Photoluminescence (PL) under 130 nW of 532 nm off-resonant excitation. An inhomogeneous-distribution full-width at half-maximum of 90(2) GHz is extracted from Gaussian fits (solid line). **e**, Photoluminescence under resonant excitation (PLE) at  $B = 0$ . A homogeneous-linewidth full-width at half-maximum of 70(5) MHz is extracted from Lorentzian fits (solid line). The inset shows the second-order resonant autocorrelation function with a Bloch-equation-based fit<sup>31</sup> (solid line).

of SiV, the first centre to be investigated in this category, namely, the SnV centre, stands out, as it possesses an intrinsically higher quantum efficiency (80% versus 10% for SiV)<sup>16,23</sup>, robustness of optical cyclicity against an applied external magnetic field<sup>17</sup> and intrinsically long coherence times above 1 K (ref. 24). In particular, the high quantum efficiency and large Debye–Waller factor relaxes the requirement of large Purcell enhancement to ameliorate the imperfect photonic efficiency and enables a waveguide-based route for a high-efficiency spin–photon interface. For a sufficiently well-coupled spin, a waveguide can also serve as a photonic gate within an all-optical quantum circuit<sup>25</sup>. Relative to nanocavities, the waveguide architecture offers a broadband platform with superior scalability<sup>26</sup>, reduced fabrication complexity and control overhead<sup>27</sup> and improved outcoupling to optical fibres<sup>13</sup>. For scalable quantum communication, the remaining challenges for the SnV centre are to demonstrate integration into such a high-photonic-efficiency platform and to establish access to long-lived nuclear memories.

In this work, we present a fibre-packaged nanophotonic waveguide device with efficient optical coupling and direct optical access to a deterministically present nuclear spin. Isotopically filtered  $^{117}\text{Sn}$  implantation results in  $^{117}\text{SnV}$  centres with optically addressable hyperfine transitions separated by 452(7) MHz. As this is 16 times greater than the optical linewidth, it enables direct optical access to the hyperfine-split states and therefore the initialization and single-shot readout of the nuclear spin. The nuclear spin can, thus, serve as an ancillary memory to the electron or as a stand-alone qubit. Interfacing the waveguide with an adiabatically tapered optical fibre results in a waveguide-to-fibre extraction efficiency of at least 57(6)%, enabling the practical detection of up to five consecutive photons, which will enable multidimensional photonic cluster-state generation<sup>28</sup>. We further show a single-photon nonlinearity conditional on the electronuclear state, which we employ as a spin-gated photonic switch. The realized integration of the  $^{117}\text{SnV}$  centre into a fibre-packaged and high-efficiency photonic device, combined with the demonstrated coherent spin control<sup>17</sup> and the intrinsically high single-photon quality<sup>15</sup>, realizes a scalable solid-state platform to advance the pursuit of quantum networks.

## Results

### A fibre-packaged nanophotonic device

Our quantum device is a diamond microchiplet coupled to a tapered optical fibre (Fig. 1a). The quantum microchiplets are formed through

isotopically selective ion implantation and subsequent top-down nanofabrication with the incorporation of a Bragg reflector in the centre of the waveguide to reflect all light towards a single adiabatically tapered port<sup>29</sup> (Supplementary Section I). A conically tapered fibre is adhered to the adiabatically tapered port of the waveguides to form a packaged device (Methods). Figure 1b illustrates this setup and the subsequent collection optics. A single, fibre-based input and output port is employed for all the measurements in this work, with no tuning requirements owing to the broadband nature of the platform. A 90:10 fibre-based beamsplitter separates the two counter-propagating modes. From reflection measurements, we extract a waveguide-to-fibre coupling efficiency greater than 57(6)% at 620 nm (Supplementary Section II), with no degradation in the coupling efficiency when the device is handled or cooled to  $\sim 0.4$  K.

Figure 1c highlights the relevant optical transitions of the SnV centre. In the absence of a magnetic field, the ground state consists of two orbital levels, each with degenerate spin sublevels<sup>30</sup>. The two transitions to a shared excited state are visible in Fig. 1d, where the  $^{117}\text{SnV}$  centre is excited with off-resonant light. For the  $^{117}\text{SnV}$  centre, the electron hyperfine interaction with the  $I = 1/2$  nucleus results in an optically resolvable splitting of the ground state into aligned and anti-aligned electronuclear spin levels. Figure 1e presents a direct measurement of the zero-field substructure, where the phonon-sideband (PSB) fluorescence is collected, whereas the excitation wavelength is scanned through the two transitions using a chirped optical resonance excitation (CORE) scheme<sup>15</sup> (Supplementary Section III). This scheme minimizes optical pumping by repeatedly scanning the laser at a constant rate over the transitions, which is  $\sim 0.2$  MHz  $\text{ns}^{-1}$  for our system. The inset shows a second-order autocorrelation function ( $g^{(2)}(0) = 0.052(4)$ ) obtained by resonantly exciting the two transitions simultaneously, verifying that this substructure results from a single  $^{117}\text{SnV}$  centre<sup>31</sup>.

### Optical access to the $^{117}\text{SnV}$ centre

When a magnetic field  $B_z$  is present along the symmetry axis of the defect (Fig. 2a), the remaining spin degeneracy is split by the electronic Zeeman effect<sup>30</sup>. Due to the forbidden nature of spin flips in electric dipole transitions<sup>30</sup>, the four visible transitions correspond to the allowed electron- and nuclear-spin-preserving transitions. As the hyperfine coupling is much stronger than the nuclear Zeeman effect, the nuclear quantization axis is strongly pinned by the electronic

quantization axis, and the ground and excited states are each described by the Hamiltonian

$$H = \gamma_S^* B_z S_z + \gamma_I B_z I_z + A_{\parallel} S_z I_z, \quad (1)$$

where  $\gamma_S^*$  is an effective electron gyromagnetic ratio;  $\mathbf{S}$  and  $\mathbf{I}$  are the electron and nuclear spin operators, respectively; and  $A_{\parallel}$  is the parallel component of the hyperfine tensor (Supplementary Section IV). The four visible spin-conserving transitions occur at detunings  $\delta \in \{\pm \Delta A_{\parallel}/4 \pm \Delta(\gamma_S^*/2)B_z\}$ , where  $\Delta$  indicates the difference between ground- and excited-state values of the respective parameter. A fit to the spectra shown in Fig. 2a yields a splitting rate of  $\Delta\gamma_S^*/2\pi = 5.41(6)$  GHz T<sup>-1</sup> and a zero-field splitting that is 15.8 times greater than the lifetime-limited optical linewidth  $\gamma_0/2\pi = 28.6(1)$  MHz (Supplementary Section V).

Figure 2b highlights that optical splitting is intrinsic to the <sup>117</sup>Sn nucleus. Across all the twelve <sup>117</sup>SnV centres measured in our device, we extract a zero-field hyperfine splitting of  $|\Delta A_{\parallel}|/4\pi = 452(7)$  MHz. This consistency is in sharp contrast with <sup>13</sup>C-based memories, whose couplings are stochastic<sup>10</sup>. Due to the split-vacancy structure of the defect, we expect this optical splitting to be dominated by the ground-state hyperfine tensor. In the even-parity ground state, the hyperfine interaction should be dominated by the Fermi contact interaction and thus be primarily isotropic<sup>32</sup>, whereas in the odd-parity excited state, the Fermi contact interaction vanishes and the dipolar contribution should result in a much smaller interaction<sup>30</sup>. As the hyperfine coupling is proportional to the nuclear gyromagnetic ratio, our measurements should extend with little modification to the other ( $I = 1/2$ ) spin-active tin isotopes, namely, <sup>115</sup>Sn and <sup>119</sup>Sn, for which we predict optical splittings of approximately 415 and 475 MHz, respectively<sup>33,34</sup>; the latter is in agreement with more recent measurements<sup>35</sup>. Another work<sup>36</sup> reported isotopic shifts in emission frequency, but no nuclear interaction. The hyperfine-split optical signature enables the future identification of different isotopes without spectrally resolving their inhomogeneous distributions. Further, the large ground-state hyperfine coupling should enable two-qubit gates at an ~20 MHz rate, as previously achieved with SiV centres<sup>19</sup>, but without the observed infidelities or overheads associated with the indirect driving of nearby transitions. Previous reports of nuclear couplings to SnV centres probably correspond to nearby <sup>13</sup>C whose couplings have been predicted in a matching range<sup>17,37</sup>.

In Fig. 2c, we utilize the optical accessibility to the hyperfine manifold to perform state initialization at a magnetic field of  $\mathbf{B} = \mathbf{0}$ . By pumping on the C1 (C2) transition, we initialize the system into the  $|0\rangle$  ( $|1\rangle$ ) state with a fidelity of 96.9(3)% (98.6(3)%) as derived from the polarization asymmetry in a subsequent CORE scan. Direct optical pumping presents a lower control overhead than typical nuclear initialization mechanisms based on electron initialization followed by a SWAP gate<sup>19</sup>, measurement-based initialization<sup>38</sup> or dynamic nuclear polarization<sup>39</sup>. This initialization protocol is potentially extendable to the other solid-state emitters with a comparable ratio of hyperfine coupling to optical linewidth such as the V<sup>4+</sup> centre in SiC (ref. 40) and the rare-earth ions in wide-bandgap semiconductors<sup>41</sup>.

Figure 2d shows a measurement of the longitudinal relaxation time, where the <sup>117</sup>SnV centre is initialized into the  $|1\rangle$  state and the polarization asymmetry is measured after a time delay. The time constant of the decay  $T_1 = 1.25(10)$  s provides a lower bound on the intrinsic nuclear polarization lifetime, as residual laser leakage may lead to additional depolarization processes. This result highlights that the nuclear spin can act as a long-lived nuclear memory where the large hyperfine splitting suppresses flip-flop interactions with the surrounding nuclear bath<sup>42,43</sup>. Given the low coupling of nuclei to phonons, it may be possible to operate a nuclear memory at higher temperatures<sup>19</sup>.

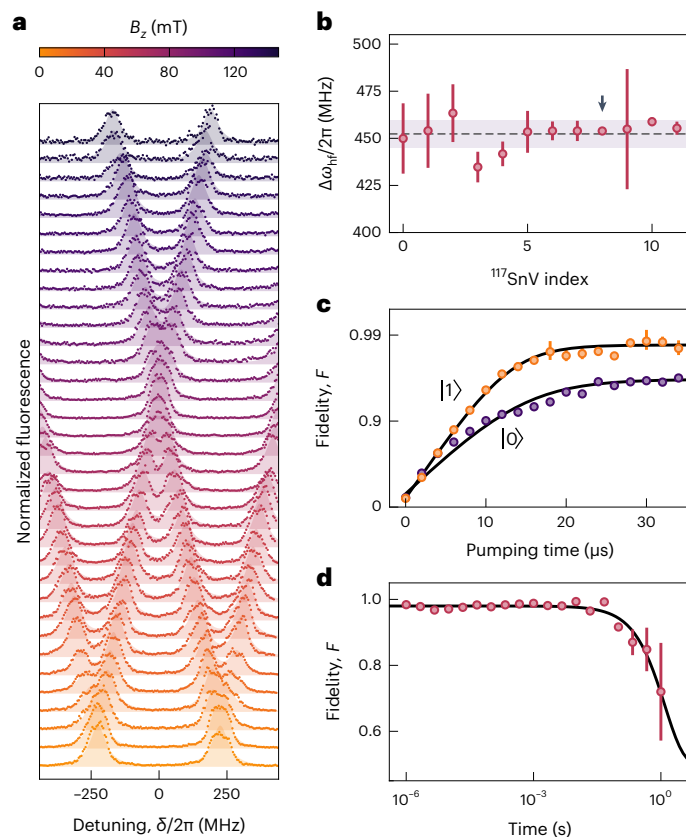


**Fig. 2 | Accessing the <sup>117</sup>SnV electronuclear spin manifold. a**, Repeated CORE scans as a function of the magnetic field along the [111] axis. The magnetic field is varied from 0 to 147.0 mT in steps of 4.3 mT. **b**, Hyperfine splitting of the optical transitions at  $\mathbf{B} = \mathbf{0}$  for multiple emitters in the waveguide. The emitter employed for all the other measurements is highlighted with an arrow. The shaded region corresponds to the standard deviation. The error bars correspond to the single standard deviation uncertainty in zero-field peak splitting from fits to the spectra. **c**, Initialization fidelity as a function of optical pumping time for the  $|0\rangle$  (purple) and  $|1\rangle$  (orange) states. The error bars correspond to the single standard deviation uncertainty in the CORE peak height from spectral fits. **d**, State fidelity as a function of time after initialization. The error bars correspond to the single standard deviation uncertainty in the peak CORE heights from spectral fits.

### An efficient optical interface

Having identified an optically resolvable nuclear substructure, we now evaluate the optical coupling of the centre to our nanostructured waveguide. Figure 3a shows a saturation curve obtained by conducting a CORE scan over the optical transitions and summing the fluorescence amplitude of the two hyperfine-split transitions. From a fit of the form  $I_{\infty}/(1 + P_{\text{sat}}/P)$  (ref. 44), we extract a power at saturation  $P_{\text{sat}} = 120(30)$  pW at the input of the adiabatically tapered fibre. This corresponds to the <sup>117</sup>SnV centre being saturated by a flux of 2.1(5) photons per lifetime, confirming an efficient light–matter interface. The maximum resonance fluorescence rate  $I_{\infty} = 1.34(5)$  Mcps is the highest achieved for SnV centres and extends beyond previous reports for SnV centres in bulk diamond (~25 kcps)<sup>45</sup> and nanopillars (81 kcps)<sup>24</sup> by over an order of magnitude.

Leveraging this efficient interface, we now demonstrate a single-shot readout of the nuclear spin through a pump–probe measurement and counting the photon arrival events. Figure 3b shows histograms of the number of photons collected in a readout pulse for the case where the qubit was initialized into the  $|0\rangle$  (purple) or  $|1\rangle$  (orange) state. The two distributions have an average photon number of  $\langle n \rangle_{|0\rangle} = 1.83$  and  $\langle n \rangle_{|1\rangle} = 0.13$ . We obtain a fidelity of  $F = 80(1)\%$ , using the optimal one-photon threshold and a readout time of 15  $\mu\text{s}$  (Fig. 3b,

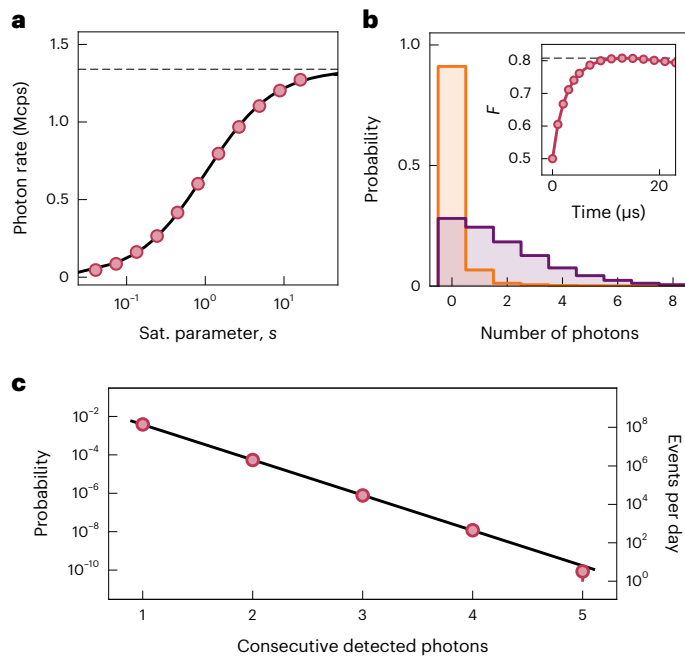


**Fig. 3 | An efficient optical interface.** **a**, PSB fluorescence as a function of saturation parameter,  $s = P/P_{\text{sat}}$ . **b**, Histogram of photon counts per readout pulse after the state is initialized into the  $|0\rangle$  (purple) or  $|1\rangle$  (orange) state. The inset shows the fidelity as a function of readout time. **c**, Probability of detecting  $N$  consecutive photons at a 0.38 MHz generation rate.

inset). Our high photon collection efficiency ultimately manifests itself in the detection of multiphoton coincidences (Fig. 3c).

Phase-sensitive and phase-insensitive remote entanglement protocols linearly and quadratically vary with the detection efficiency, respectively<sup>46</sup>. For the latter, the two-photon detection probability of  $5.065(4) \times 10^{-5}$  sets an ultimate rate limit of  $\sim 0.7$  kHz for Bell-pair entanglement generation. We further highlight the detection of multiple five-photon coincidence events in a 24 h time period. The high overall detection efficiency of 1.40(5)%, thus, brings to light the possibility of generating complex entanglement resources, such as graph states. In particular, five-photon graph states have been proposed to enable measurement-based error-tolerant quantum communication<sup>47</sup>. More generally, as cluster states only differ from the well-studied Greenberger–Horne–Zeilinger (GHZ) states when consisting of at least four photons<sup>6</sup>, this enables a new experimental regime.

When paired with high-purity zero-phonon-line (ZPL) photon collection efficiencies recently demonstrated for SnV centres in the waveguide architecture used in this work<sup>15</sup>, the path to photonic cluster states becomes accessible in the near term. Improvements in collection efficiency could be realized through the use of superconducting nanowire single-photon detectors and improvements to the adiabatic mode transfer through optimized fabrication protocols, further enhancing the complexity of the entanglement resources achievable with the <sup>117</sup>SnV centre (Supplementary Section II). Such improvements may bring the class-leading collection efficiencies achieved with diamond nanocavities<sup>13</sup> to a low-overhead waveguide platform, without cryostatic alignment, confocal excitation or cavity tuning.

### A spin-gated optical switch

We now combine our controllable electronuclear state with our high-efficiency light–matter interface. Figure 4a,b shows the PSB fluorescence and resonant reflection data, respectively, collected from a CORE scan across the two hyperfine-split transitions after the electronuclear register is initialized into the  $|0\rangle$  (purple) or  $|1\rangle$  (orange)

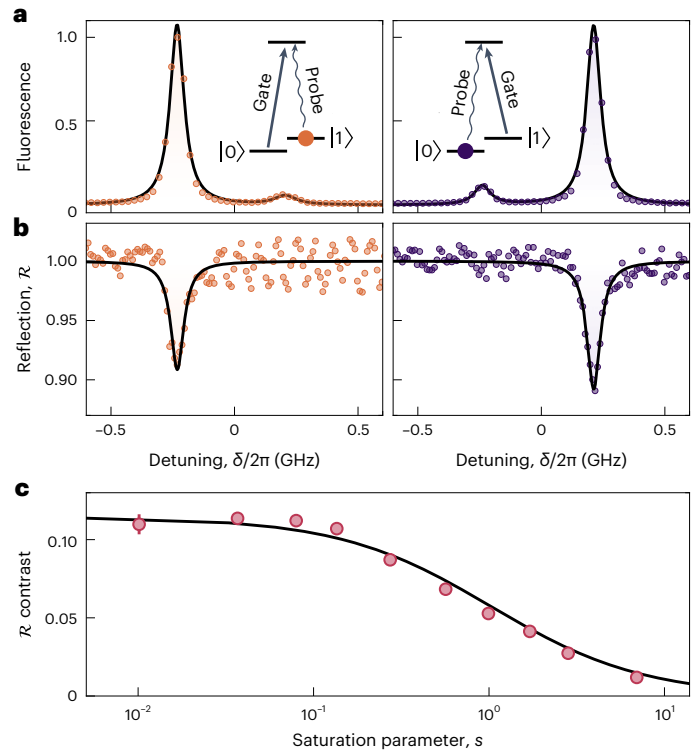


**Fig. 4 | A spin-gated optical switch.** **a**, PSB fluorescence as a function of probe detuning after the emitter has been pumped by a gate pulse into the  $|0\rangle$  (purple) and  $|1\rangle$  (orange) states. **b**, Reflection intensity as a function of detuning. **c**, Contrast of the resonant reflection dip as a function of saturation parameter,  $s$ . The presented reflection contrast is the mean of the contrast of the two transitions.

state, and corrected for spectral diffusion (Supplementary Section III). In Fig. 4b, we observe a decrease in reflectivity, with up to 11(1)% contrast, as the resonant laser probe field is brought onto single-photon resonance with the two transitions after initialization. This is a characteristic signature of high-efficiency coupling in waveguide quantum electrodynamics<sup>48</sup>. Importantly, this nonlinearity is conditional on the spin state of the electronuclear manifold and thus acts as a spin-gated photonic switch. The saturability of the nonlinear response (Fig. 4c) is a signature of the non-classical character of the nonlinearity. This opens up a pathway for memory-enhanced quantum communication<sup>49</sup>, in combination with photonic crystal cavities<sup>50</sup>, or photon–photon spin-mediated interactions<sup>25</sup>, and Fock-state readout using the <sup>117</sup>SnV centre<sup>25</sup>.

A fit to the reflection contrast can be employed to characterize the efficiency of the spin–photon interface. Specifically, for a two-level system in a broadband cavity, the reflectivity coefficient for near-resonant light is given by

$$r(\omega) = 1 - \frac{2f}{1 + C/(1 + 2i\delta/\gamma_h)}, \quad (2)$$

where  $C$  is the cooperativity;  $\gamma_h$ , the homogeneous linewidth of the <sup>117</sup>SnV centre;  $\delta$ , the detuning of the probe field; and  $f$ , the fraction of cavity photons that exit towards the input port of the cavity (Supplementary Section VI). The cooperativity is related to  $\beta_{\text{tot}}$ , defined as the ratio of ZPL emission into the waveguide mode to the total population decay rate. From a fit of the measured power reflectivity,  $\mathcal{R} = |r|^2$ , we extract  $\beta_{\text{tot}} > 6.2(7)\%$ .

The  $\beta$ -factor measured in Fig. 4c can be decomposed into the product of the intrinsic  $\beta$ -factor of the waveguide ( $\beta_{\text{wg}}$ ), the internal

quantum efficiency ( $\eta_{QE}$ ), the Debye–Waller factor ( $\eta_{DW}$ ) and ZPL orbital branching ratio ( $\eta_{orb}$ ) as  $\beta_{tot} = \beta_{wg} \times \eta_{QE} \times \eta_{DW} \times \eta_{orb}$ . A higher  $\beta$ -factor could be realized through (1) improved centre positioning, as can be achieved through shallow implantation and subsequent overgrowth<sup>51</sup>; (2) improved emission dipole alignment, achievable through the use of <111>-oriented diamond in fabrication; or (3) Purcell enhancement, as has been previously achieved for the SnV centre in nanocavities<sup>50</sup>. This decomposition further constrains the quantum efficiency of the SnV centre to be  $\eta_{QE} > 51(8)\%$ . This is compatible with theoretical calculations (91%)<sup>52</sup> and previous rate-equation measurements (79%) and represents an intrinsic advantage of SnV over SiV, for which the quantum efficiency is in the range of 5–10% (refs. 16, 53). A large quantum efficiency results in a higher cooperativity factor for a given scattering loss rate, fixed by fabrication imperfections, and thus lessens the challenge of efficient photonic outcoupling present for critically coupled nanocavities<sup>13</sup>.

## Discussion

In this work, we have introduced a versatile quantum device, consisting of a fibre-packaged waveguide with access to a nuclear spin that serves to address three key challenges for optically interconnected qubit systems. First, as a quantum node, the high waveguide-to-fibre extraction efficiency of 57(6)% should enable high-repetition-rate remote entanglement based on single-photon protocols when combined with previous demonstrations of quantum control<sup>17</sup> and interference of resonant photons<sup>15</sup>. This entanglement generation rate would be limited by initialization and readout overheads in the current device, which could be lowered through fast-feedback control logic<sup>19</sup>. For entanglement distribution over more than two nodes, an ancillary register is necessary<sup>54</sup>. The immediate next steps, thus, involve microwave control of the nuclear state<sup>19</sup>, echoing recent demonstrations of high-fidelity electron control<sup>55,56</sup>. The large hyperfine coupling is advantageous to realize fast two-qubit gates without the typical infidelities associated with the indirect driving of nearby transitions<sup>19</sup>. The protected nature of the nuclear spin should enable a second-long coherence time<sup>19</sup>. Finally, addressing nearby <sup>13</sup>C through dynamical decoupling gates is a natural way to extend this register<sup>10</sup> to realize fault-tolerant nodes.

Second, as a source for photonics cluster states, the detection of five-photon events in a 24 h period showcases the feasibility of proof-of-principle demonstrations, particularly when combined with a nuclear memory<sup>28</sup>. Large-scale cluster-state generation, as required for efficient and scalable quantum computing<sup>57</sup>, would require near-unity overall detection efficiency and thus integration into a nanocavity<sup>13</sup> or open microcavity<sup>2</sup>, but the current device is already sufficient for first demonstrations.

Third, as a gate for photonic logic, the single-photon nonlinearly presented in this work is a quantum resource on its own. A higher reflection contrast would enable reflection-based spin readout<sup>19</sup> and high-contrast spin-gated photonic switching. Its combination with coherent Raman control would enable a single-photon transistor<sup>58</sup>. Deterministic photon–photon logic gates in combination with large-scale integration into photonic integrated circuits could serve to reduce the exponential overhead of linear optical quantum computing protocols<sup>59</sup>. Ultimately, the combination of a low-overhead and high-efficiency photonic interface, optically addressable deterministic nuclear register that is intrinsic to all <sup>117</sup>SnV colour centres and integration into a scalable platform represents a novel resource in the pursuit of quantum networking.

## Online content

Any methods, additional references, Nature Portfolio reporting summaries, source data, extended data, supplementary information, acknowledgements, peer review information; details of author contributions and competing interests; and statements of data and code availability are available at <https://doi.org/10.1038/s41566-023-01332-8>.

## References

- Kimble, H. J. The quantum internet. *Nature* **453**, 1023–1030 (2008).
- Tomm, N. et al. A bright and fast source of coherent single photons. *Nat. Nanotechnol.* **16**, 399–403 (2021).
- Uppu, R. et al. Scalable integrated single-photon source. *Sci. Adv.* **6**, eabc8268 (2020).
- Javadi, A. et al. Spin-photon interface and spin-controlled photon switching in a nanobeam waveguide. *Nat. Nanotechnol.* **13**, 398–403 (2018).
- Delteil, A. et al. Generation of heralded entanglement between distant hole spins. *Nat. Phys.* **12**, 218–223 (2016).
- Istrati, D. et al. Sequential generation of linear cluster states from a single photon emitter. *Nat. Commun.* **11**, 5501 (2020).
- Zaporski, L. et al. Ideal refocusing of an optically active spin qubit under strong hyperfine interactions. *Nat. Nanotechnol.* **18**, 257–263 (2023).
- Denning, E. V., Gangloff, D. A., Atatüre, M., Mørk, J. & Le Gall, C. Collective quantum memory activated by a driven central spin. *Phys. Rev. Lett.* **123**, 140502 (2019).
- Bar-Gill, N., Pham, L. M., Jarmola, A., Budker, D. & Walsworth, R. L. Solid-state electronic spin coherence time approaching one second. *Nat. Commun.* **4**, 1743 (2013).
- Bradley, C. E. et al. A ten-qubit solid-state spin register with quantum memory up to one minute. *Phys. Rev. X* **9**, 031045 (2019).
- Johnson, S. et al. Tunable cavity coupling of the zero phonon line of a nitrogen-vacancy defect in diamond. *New J. Phys.* **17**, 122003 (2015).
- Hermans, S. et al. Qubit teleportation between non-neighbouring nodes in a quantum network. *Nature* **605**, 663–668 (2022).
- Knall, E. N. et al. Efficient source of shaped single photons based on an integrated diamond nanophotonic system. *Phys. Rev. Lett.* **129**, 053603 (2022).
- Bhaskar, M. K. et al. Quantum nonlinear optics with a germanium-vacancy color center in a nanoscale diamond waveguide. *Phys. Rev. Lett.* **118**, 223603 (2017).
- Martínez, J. A. et al. Photonic indistinguishability of the tin-vacancy center in nanostructured diamond. *Phys. Rev. Lett.* **129**, 173603 (2022).
- Sukachev, D. D. et al. Silicon-vacancy spin qubit in diamond: a quantum memory exceeding 10 ms with single-shot state readout. *Phys. Rev. Lett.* **119**, 223602 (2017).
- Debroux, R. et al. Quantum control of the tin-vacancy spin qubit in diamond. *Phys. Rev. X* **11**, 041041 (2021).
- Nguyen, C. et al. An integrated nanophotonic quantum register based on silicon-vacancy spins in diamond. *Phys. Rev. B* **100**, 165428 (2019).
- Stas, P.-J. et al. Robust multi-qubit quantum network node with integrated error detection. *Science* **378**, 557–560 (2022).
- Rugar, A. E. et al. Narrow-linewidth tin-vacancy centers in a diamond waveguide. *ACS Photonics* **7**, 2356–2361 (2020).
- Evans, R. E. et al. Photon-mediated interactions between quantum emitters in a diamond nanocavity. *Science* **362**, 662–665 (2018).
- Sipahigil, A. et al. An integrated diamond nanophotonics platform for quantum-optical networks. *Science* **354**, 847–850 (2016).
- Iwasaki, T. et al. Tin-vacancy quantum emitters in diamond. *Phys. Rev. Lett.* **119**, 253601 (2017).
- Trusheim, M. E. et al. Transform-limited photons from a coherent tin-vacancy spin in diamond. *Phys. Rev. Lett.* **124**, 023602 (2020).
- Le Jeannic, H. et al. Dynamical photon–photon interaction mediated by a quantum emitter. *Nat. Phys.* **18**, 1191–1195 (2022).
- Wan, N. H. et al. Large-scale integration of artificial atoms in hybrid photonic circuits. *Nature* **583**, 226–231 (2020).

27. Douglas, J. S. et al. Quantum many-body models with cold atoms coupled to photonic crystals. *Nat. Photon.* **9**, 326–331 (2015).
28. Michaels, C. P. et al. Multidimensional cluster states using a single spin-photon interface coupled strongly to an intrinsic nuclear register. *Quantum* **5**, 565 (2021).
29. Mouradian, S., Wan, N. H., Schröder, T. & Englund, D. Rectangular photonic crystal nanobeam cavities in bulk diamond. *Appl. Phys. Lett.* **111**, 021103 (2017).
30. Hepp, C. et al. Electronic structure of the silicon vacancy color center in diamond. *Phys. Rev. Lett.* **112**, 036405 (2014).
31. Kim, J. & Noh, H.-R. Analytical solutions of the second-order correlation function in resonance fluorescence for two-level systems. *J. Korean Phys. Soc.* **76**, 463–468 (2020).
32. McConnell, H. M. & Robertson, R. E. Isotropic nuclear resonance shifts. *J. Chem. Phys.* **29**, 1361–1365 (1958).
33. Laaksonen, A. & Wasylishen, R. E. An absolute chemical shielding scale for tin from NMR relaxation studies and molecular dynamics simulations. *J. Am. Chem. Soc.* **117**, 392–400 (1995).
34. Lassigne, C. R., Wells, E., Farrugia, L. J. & James, B. R. Heteronuclear second-order coupling effects in high-resolution tin NMR spectra. *J. Magn. Reson.* **43**, 488–490 (1981).
35. Harris, I. B. et al. Hyperfine spectroscopy of isotopically engineered group-IV color centers in diamond. *PRX Quantum* **4**, 040301 (2023).
36. Narita, Y. et al. Multiple tin-vacancy centers in diamond with nearly identical photon frequency and linewidth. *Phys. Rev. App.* **19**, 024061 (2023).
37. Defo, R. K., Kaxiras, E. & Richardson, S. L. Calculating the hyperfine tensors for group-IV impurity-vacancy centers in diamond using hybrid density functional theory. *Phys. Rev. B* **104**, 075158 (2021).
38. Waldherr, G. et al. Quantum error correction in a solid-state hybrid spin register. *Nature* **506**, 204–207 (2014).
39. Scheuer, J. et al. Optically induced dynamic nuclear spin polarisation in diamond. *New J. Phys.* **18**, 013040 (2016).
40. Wolfowicz, G. et al. Vanadium spin qubits as telecom quantum emitters in silicon carbide. *Sci. Adv.* **6**, eaaz1192 (2020).
41. Zhong, T. et al. Nanophotonic rare-earth quantum memory with optically controlled retrieval. *Science* **357**, 1392–1395 (2017).
42. Merkulov, I., Efros, A. L. & Rosen, M. Electron spin relaxation by nuclei in semiconductor quantum dots. *Phys. Rev. B* **65**, 205309 (2002).
43. Seo, H. et al. Quantum decoherence dynamics of divacancy spins in silicon carbide. *Nat. Commun.* **7**, 12935 (2016).
44. Radulaski, M. et al. Scalable quantum photonics with single color centers in silicon carbide. *Nano Lett.* **17**, 1782 (2017).
45. Görlitz, J. et al. Coherence of a charge stabilised tin-vacancy spin in diamond. *npj Quantum Inf.* **8**, 45 (2022).
46. Stockill, R. et al. Phase-tuned entangled state generation between distant spin qubits. *Phys. Rev. Lett.* **119**, 010503 (2017).
47. Zwerger, M., Briegel, H. & Dür, W. Measurement-based quantum communication. *Appl. Phys. B* **122**, 50 (2016).
48. Grangier, P., Raymond, G. & Schlosser, N. Implementations of quantum computing using cavity quantum electrodynamics schemes. In *Scalable Quantum Computers: Paving the Way to Realization* <https://doi.org/10.1002/3527603182.ch7> (2000).
49. Bhaskar, M. K. et al. Experimental demonstration of memory-enhanced quantum communication. *Nature* **580**, 60–64 (2020).
50. Rugar, A. E. et al. Quantum photonic interface for tin-vacancy centers in diamond. *Phys. Rev. X* **11**, 031021 (2021).
51. Rugar, A. E. et al. Generation of tin-vacancy centers in diamond via shallow ion implantation and subsequent diamond overgrowth. *Nano Lett.* **20**, 1614–1619 (2020).
52. Thiering, G. & Gali, A. Ab initio magneto-optical spectrum of group-IV vacancy color centers in diamond. *Phys. Rev. X* **8**, 021063 (2018).
53. Neu, E., Agio, M. & Becher, C. Photophysics of single silicon vacancy centers in diamond: implications for single photon emission. *Opt. Express* **20**, 19956–19971 (2012).
54. Pompili, M. et al. Realization of a multi-node quantum network of remote solid-state qubits. *Science* **372**, 259–264 (2021).
55. Rosenthal, E. I. et al. Microwave spin control of a tin-vacancy qubit in diamond. *Phys. Rev. X* **13**, 031022 (2023).
56. Guo, X. et al. Microwave-based quantum control and coherence protection of tin-vacancy spin qubits in a strain-tuned diamond membrane heterostructure. Preprint at <https://arxiv.org/abs/2307.11916> (2023).
57. Raussendorf, R. & Briegel, H. J. A one-way quantum computer. *Phys. Rev. Lett.* **86**, 5188 (2001).
58. Chang, D. E., Sørensen, A. S., Demler, E. A. & Lukin, M. D. A single-photon transistor using nanoscale surface plasmons. *Nat. Phys.* **3**, 807–812 (2007).
59. Knill, E., Laflamme, R. & Milburn, G. J. A scheme for efficient quantum computation with linear optics. *Nature* **409**, 46–52 (2001).

**Publisher's note** Springer Nature remains neutral with regard to jurisdictional claims in published maps and institutional affiliations.

**Open Access** This article is licensed under a Creative Commons Attribution 4.0 International License, which permits use, sharing, adaptation, distribution and reproduction in any medium or format, as long as you give appropriate credit to the original author(s) and the source, provide a link to the Creative Commons license, and indicate if changes were made. The images or other third party material in this article are included in the article's Creative Commons license, unless indicated otherwise in a credit line to the material. If material is not included in the article's Creative Commons license and your intended use is not permitted by statutory regulation or exceeds the permitted use, you will need to obtain permission directly from the copyright holder. To view a copy of this license, visit <http://creativecommons.org/licenses/by/4.0/>.

Springer Nature or its licensor (e.g. a society or other partner) holds exclusive rights to this article under a publishing agreement with the author(s) or other rightsholder(s); author self-archiving of the accepted manuscript version of this article is solely governed by the terms of such publishing agreement and applicable law.

© The Author(s) 2023

## Methods

### Waveguide microchiplet fabrication

An electronic-grade diamond (Element Six, [N] < 5 ppb) was first chemically polished via ArCl<sub>2</sub> reactive ion etching to smooth the surface to <1 nm roughness and then implanted with <sup>117</sup>Sn<sup>++</sup> ions twice. The first implantation (Cutting Edge Ions) used an implantation energy of 200 keV and a dosage of 5 × 10<sup>10</sup> ions cm<sup>-2</sup>, whereas the second implant occurred at a dosage of 1 × 10<sup>11</sup> ions cm<sup>-2</sup> and 350 keV implantation energy (86 nm implant depth; 17 nm straggle). The second implantation was needed as SnV photoluminescence was not observed after the initial implantation and subsequent high-temperature anneal. Following the second implantation, the diamond was annealed at 1,200 °C for 12 h at ~10<sup>-7</sup> mbar followed by a boiling tri-acid clean (nitric, sulfuric and perchloric acids mixed in a 1:1:1 ratio and heated to 345 °C). Quantum microchiplets<sup>26</sup>, each containing eight waveguide channels, were fabricated in bulk diamond through quasi-isotropic etching<sup>29</sup> and subsequent high-temperature annealing, again at 1,200 °C for 12 h followed further by a boiling tri-acid clean. Finally, the diamond was submerged in a piranha solution (sulfuric acid mixed with hydrogen peroxide in a 3:1 ratio) to improve surface termination<sup>60</sup>. Chiplets were then picked and placed onto the edge of a fused silica substrate to enable fibre-based optical access<sup>15</sup> (Supplementary Section I).

### Tapered fibre fabrication

A standard single-mode optical fibre (Thorlabs SM600) is first mechanically stripped and cleaved. Conically tapered fibres are then fabricated through dynamic meniscus etching in hydrofluoric acid<sup>61,62</sup> using an 80 ml solution of 40% hydrofluoric acid and 10 ml of *ortho*-xylene. A set of six fibres is lowered into the solution and progressively retracted at 55 μm min<sup>-1</sup> over the course of 95 min, yielding a conical half-angle of 1.5(8)°. A fibre is then coated with a thin layer of photopolymerized optical adhesive (Norland Optical Adhesive 86H) and adhered to the adiabatically tapered port of a waveguide<sup>63</sup>. The final device is then mounted inside the cryostat employed in this work such that the diamond end of the fibre is free floating, mechanically held in place through the fibre input–output port (Supplementary Section I). Finally, the cryostat is cooled to ~0.4 K, where the sample temperature is monitored by a sensor thermally anchored to the gold-plated copper block affixing the fibre.

### Laser control setup

We employ a tunable resonant source at 619 nm (M-Squared Lasers, SolsTiS + EMM) for all our experiments. The off-resonant source at 532 nm is only employed for the measurements of photoluminescence and is not required during on-resonance measurements to initialize the charge state of the emitter<sup>45</sup>. Resonant light is found to be sufficient to initialize the charge state. The resonant light is directed through an acousto-optic modulator (Gooch and Housego 3080-15) and a fibre-based electro-optic modulator (EOM; Jenoptik AM635). The EOM is used for all-optical pulsing and is controlled by a 25 Gsamples s<sup>-1</sup> arbitrary waveform generator (Tektronix AWG70002A) through a microwave amplifier (Minicircuits ZX60-83LN12+) and a bias-tee (Minicircuits ZFBT-6G+). The resonant laser is detuned by 3.5 GHz from the middle point of the C1 and C2 transitions to minimize the laser excitation caused by leakage laser light, and near-resonant light is generated through the sinusoidal modulation of the EOM with a frequency swept around 3.5 GHz. In all the resonant measurements, the EOM is stabilized to its interferometric minimum through a lock-in amplifier and proportional–integral–derivative (PID) loop (Red Pitaya, STEMLab 125-10). A pulse generator (Swabian Instruments Pulse Streamer 8/2) is employed as a master clock to coordinate all the instruments (Supplementary Section III).

### Spectral drift compensation

The <sup>117</sup>SnV centres investigated in this work show a slow (~10 min time-scale) spectral diffusion over an ~100 MHz spectral range. We actively

correct for this drift by conducting a 5 s CORE scan every 60 s to compensate the drifting zero-detuning ( $\delta = 0$ ) position of the <sup>117</sup>SnV centres. In Fig. 4, we instead recentre the drift in the data analysis by overlapping consecutive 1 min scans based on Lorentzian fits. We further note that in contrast to the data in Fig. 4a,b, the qubit is not prepared into either the |0⟩ or |1⟩ states (Fig. 4c). This is due to the difficulty in consistently initializing the spin as the excitation power is scanned over three orders of magnitude (10<sup>-2</sup> < *s* < 10<sup>1</sup>). As such, the sum of the two reflection dips is taken as the nonlinearity contrast.

### Data availability

The data that support the findings of this study are available from the corresponding authors on reasonable request.

### References

60. Sangtawesin, S. et al. Origins of diamond surface noise probed by correlating single-spin measurements with surface spectroscopy. *Phys. Rev. X* **9**, 031052 (2019).
61. Haber, L., Schaller, R., Johnson, J. & Saykally, R. Shape control of near-field probes using dynamic meniscus etching. *J. Microsc.* **214**, 27–35 (2004).
62. Burek, M. J. et al. Fiber-coupled diamond quantum nanophotonic interface. *Phys. Rev. Appl.* **8**, 024026 (2017).
63. Wasserman, W. et al. Cryogenic and hermetically sealed packaging of photonic chips for optomechanics. *Opt. Express* **30**, 30822–30831 (2022).

### Acknowledgements

We would like to thank M. Tribble for fruitful discussions. We acknowledge support from the ERC Advanced Grant PEDESTAL (884745), the EU Quantum Flagship 2D-SIPC. J.A.M. acknowledges support from the Winton Programme and EPSRC DTP; R.A.P., from the General Sir John Monash Foundation; K.C.C., from the MITRE program; C.P.M., from the EPSRC DTP; A.M.S., from EPSRC/NQIT; and M.E.T., from the Army Research Laboratory ENIAC Distinguished Postdoctoral Fellowship. D.E. acknowledges further support by the MITRE Quantum Moonshot Program.

### Author contributions

R.A.P. and J.A.M. conceived and designed the experiments. R.A.P. and J.A.M. performed the experiments with inputs from A.M.S., C.P.M., M.H.A., C.M.P. and W.G.R. J.A.M. performed the finite-difference time-domain simulations. R.A.P., J.A.M. and I.B.H. analysed the data. K.C.C. and I.B.H. fabricated the quantum microchiplet. R.A.P. and A.M.S. fabricated the tapered fibre. R.A.P. assembled the packaged device. R.A.P., J.A.M., M.E.T., D.E. and M.A. wrote the paper with input from all authors.

### Competing interests

The authors declare no competing interests.

### Additional information

**Supplementary information** The online version contains supplementary material available at <https://doi.org/10.1038/s41566-023-01332-8>.

**Correspondence and requests for materials** should be addressed to Dirk Englund or Mete Atatüre.

**Peer review information** *Nature Photonics* thanks Weibo Gao and the other, anonymous, reviewer(s) for their contribution to the peer review of this work.

**Reprints and permissions information** is available at [www.nature.com/reprints](http://www.nature.com/reprints).